Adaptive building roof combining variable transparency shape-stabilized phase change material: Application potential and adaptability in different climate zones

Pengcheng Wang [a,b], Zhongbing Liu [a,b,*], Xiaoyang Zhang [a,b], Hangming Zhang [a,b], Xi Chen [a,b], Ling Zhang [a,b]

[a] College of Civil Engineering, Hunan University, Changsha, 410082, PR China
[b] Key Laboratory of Building Safety and Energy Efficiency of Ministry of Education, Hunan University, Changsha, 410082, PR China

ARTICLE INFO

ABSTRACT

The development of adaptive building envelopes to achieve building energy efficiency is significant for reducing carbon emissions. This study proposed an adaptive building roof by utilizing the variable transparency characteristics of shape-stabilized phase change material. The envelope can regulate solar absorptivity in response to changes in ambient temperature to reduce unexpected heat gain or heat loss. A mathematical model was developed and verified by experiments. On this basis, the impacts of key parameters, including the melting temperature, thickness, extinction coefficient of phase change material, and the reflectivity of reflective film, on the envelope performance were investigated. Finally, the typical daily, seasonal and annual dynamic performance was compared between the new roof and the common insulation roof in different climate zones. The results show that the optimal melting temperature and thickness of the phase change material are 24 °C and 8 mm in Beijing, 24 °C and 4 mm in Changsha and Guangzhou, and 21 °C and 5 mm in Urumqi. In the four cities, the optimal extinction coefficients of the phase change material in the transparent/opaque state are 10 m^{-1} and 250m^{-1} and the optimal reflectivity of reflective film is 0.95. In Beijing, Changsha, Guangzhou, and Urumqi, the cumulative annual loads are 55 kWh/m^2, 42 kWh/m^2, 22 kWh/m^2, and 85 kWh/m^2, respectively. The corresponding energy-saving rates are 14.06%, 17.65%, 31.25%, and 9.57%. The new roof has better performance in Cwa and Cfa climate areas. This study provides theoretical guidance for the application and optimization of the new roof in different climatic regions.

1. Introduction

With the growing urbanization and severe climate change, building sectors are required to satisfy the increasing demands for low-carbon, sustainability, and green. According to the latest statistics [1], more than one-third of global final energy consumption and nearly 40% of CO_2 emissions are attributed to the building and construction sector, and HVAC accounts for 52% of the energy cost in residential buildings. However, the performances (e.g. airtightness and thermal insulation) of traditional building envelopes are insufficient to cope with severe climate change [2,3]. The increased requirements for indoor thermal comfort also pose challenges to building envelopes [4]. Therefore, the development of new building envelopes is significant for resisting climate change and improving the living environment.

As a new building envelope, adaptive building envelopes (ABEs) have received extensive attention [5,6]. The ABE was defined as 'A building envelope has the ability to repeatedly and reversibly change some of its functions, features or behavior over time in response to changing performance requirements and variable boundary conditions, and does this with the aim of improving overall building performance' [7]. Two design strategies were commonly used to realize the 'adaptive' of buildings: (1) dynamic operation or intelligent control [8,9]; (2) material properties alteration [10,11]. For the first design strategy, components with automatic or manual controls were often added to buildings [9,12]. Authors in Ref. [13] studied a self-adaptive building-integrated photovoltaic-thermoelectric wall system. This system can dynamically transform solar power into direct electricity and then trigger the thermoelectric radiant panel for surface temperature control. The results showed that the system could significantly reduce the annual

---

Abbreviation

ABE   adaptive building envelope
ABR   adaptive building roof
PCM   phase change material
SL-PCM   solid-liquid PCM
SS-PCM   shape-stabilized PCM
VTSS-PCM   shape-stabilized PCM with variable transparency
CIR   common insulation roof
ESR   energy saving rate
ESRE   energy storage and release efficiency
RMSE   root mean square error
CV   coefficient of variation
CAL   cumulative annual load
CML   cumulative monthly load

Nomenclature

H specific enthalpy ($kJ \cdot kg^{-1}$)
I solar radiation ($W \cdot m^{-2}$)
C specific heat ($J \cdot kg^{-1} \cdot K^{-1}$)
h heat transfer coefficient ($W \cdot m^{-2} \cdot K^{-1}$)
Q_l latent heat ($kJ \cdot kg^{-1}$)
T temperature (K)
q heat flux ($W \cdot m^{-2}$)
Q_{co} annual cooling load ($kWh \cdot m^{-2}$)
Q_{he} annual heating load ($kWh \cdot m^{-2}$)
E extinction coefficient (m^{-1})
ET extinction coefficient of VTSS-PCM in transparent state
EO extinction coefficient of VTSS-PCM in opaque state
RR reflectivity of reflective film
N number of sub-layers
L thickness

r reflectivity of each interface

Greek symbols

λ thermal conductivity ($W \cdot m^{-1} \cdot K$)
ε infrared emissivity
σ Stefan-Boltzmann constant
Δ value difference
ρ density ($kg \cdot m^{-3}$)
θ angle (rad)
ψ solar absorptivity
ξ transmittance
α forward equivalent transmittance
β forward equivalent reflectivity

Subscripts

c condensing
m melting
1   Exterior cement mortar
2   Autoclaved aerated concrete
3   interior cement mortar
4   Reflective film
5   VTSS-PCM
i indoor
o outdoor/opaque
t Total/transparent
k kth interface
s scattered radiation
co cooling
he heating
j sequence of numbers
sky sky dome

heating/cooling load. A study in Ref. [14] proposed a switchable insulation system for building roofs. They described the modeling approach and control strategies of the system. The result showed that the switchable roof insulation could reduce up to 54% of annual cooling energy use for residences. Although the ABE with dynamic operational control exhibits good energy-saving potential, its environmental and economic impacts are still unclear. Besides, this type of ABE must consist of three essential elements: sensors, processors, and actuators. Using dynamic control systems and sensor devices is not a simple and effective way to achieve energy savings in buildings.

The second design strategy always relies on advanced materials. Phase change materials (PCMs) embedded in buildings can tune their thermo-physical nature in response to weather stimuli. Thus, the PCM is suitable for designing ABE [15,16]. Li et al. [17] proposed a Trombe-wall with a PCM-encapsulated porous heat storage system. The Trombe-wall responded to the outdoor temperature through the PCM to control the wall heat flow. The result showed that the thermal efficiency of the wall was 76.2%. In different climatic conditions in China, authors in Ref. [18] studied an ABE integrated with thermochromic material and PCM. The result showed that the ABR saved up to 17% of total energy use, especially in mild climates. The PCM layer was recommended to be placed inside the roof insulation in this research. Qiao et al. [19] investigated the thermal performances of PCM wallboard in different climatic regions. The experimental results indicated that the temperature attenuation ratio of the PCM wallboard was dependent on local meteorological parameters. Zhou et al. [20] proposed a new PCM integrated Trombe-wall with passive and active cooling and hybrid ventilation. The energy storage and release efficiency (ESRE) was calculated to show the energy-saving potential of the system during both cooling and heating periods. The result showed that high-reflective or high-absorptive coating on the exterior PCM wallboard increased ESRE by 10% in summer and 13% in winter.

Most studies improve the 'adaptive' by embedding solid-liquid PCM (SL-PCM) in building envelopes through literature review. However, none of these envelopes can directly regulate solar heat gain because the SL-PCM must be encapsulated. Research in Refs. [21,22] reported a variety of shape-stabilized PCMs (SS-PCMs) to avoid the problem of leakage, some of which also undergo a change from opaque to transparent during the phase change [23]. Thus, the SS-PCM with variable transparency (VTSS-PCM) can be used to realize passive regulation of solar heat gain in buildings. A study in Ref. [24] numerically investigated an ABE system using a thin polymeric SS-PCM layer as a coating onto a highly reflective exterior façade. The results showed that the ABE reduced solar heat gain by 38% during the average warmest week in the central Massachusetts climate. However, this study lacked experiments to verify the feasibility and robustness of the system. A comprehensive overview of potential energy savings and system performance trends over an annual period was also missing. In our near work [25], a novel adaptive building roof (ABR) combining VTSS-PCM was proposed. The ABR can regulate the solar heat gain according to changes in the transparency of VTSS-PCM. Furthermore, key factors were determined by global sensitivity analysis. However, further research is required to reveal the impact of various parameters on the annual and seasonal performance of the ABR. Besides, the performance of ABR is dependent on local meteorological parameters. Thus, the energy-saving potential and climate adaptability assessment of ABR can also be a worthwhile investigation.

To this goal, we developed the model of ABR that reflects the dependence of the optical properties of the VTSS-PCM on temperature. Then, the model was verified by experiments on summer and winter
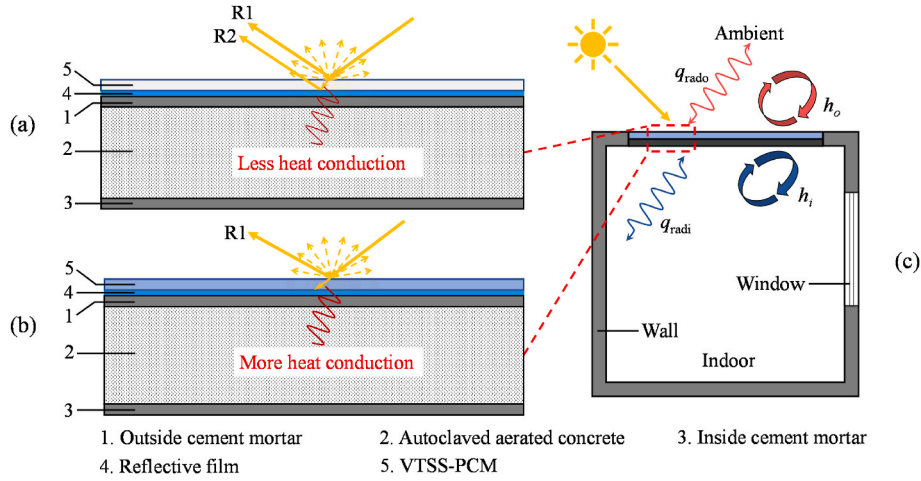
Fig. 1. Schematic diagram of the working principles of ABR: (a) summer working principle; (b) winter working principle; (c) the application of the ABR in a room. R1: primary reflection; R2: secondary reflection.

days, respectively. Under four climatic conditions in China, the effect of various factors, including the optical parameters, thermo-physical parameters, and structural parameters, on the seasonal and annual energy performance of ABR was investigated. We suggested design parameters of ABR for different climatic regions to achieve the best performance. Finally, compared with a common insulation roof (CIR), we looked at how ABR performed on a typical day, seasonal and annual. This study aims to provide theoretical guidance for the application and optimization of ABR in different climatic regions.

2. Working principles of ABR

Fig. 1 (a) and (b) show the working principles of ABR in summer and winter. Fig. 1 (c) depicts the application of the ABR in a room. From Fig. 1, the ABR consists of the VISS-PCM layer, a reflective film, outside cement mortar, autoclaved aerated concrete, and the inside cement mortar from top to bottom. In fact, the outside cement mortar, autoclaved aerated concrete, and the inside cement mortar make up the CIR, which is a typical roof used in China. Fig. 1(c) shows the heat transfer process of ABR in a building, including the heat transport through heat conduction and convection as well as radiation.

From Fig. 1 (a), at high temperatures on summer days, the VTSS-PCM transforms into an amorphous and transparent state. At this time, the reflective film is exposed to the light beam, thus the light beam can undergo the secondary reflection (R2) on the reflective film after the primary reflection (R1) on the outer surface of the VTSS-PCM layer. The light beam undergoes two reflection processes in the ABR, which means less solar radiation is converted into heat when passing through the VTSS-PCM layer. Therefore, the exterior surface temperature of ABR is decreased and the heat conduction to the room through the ABR is reduced. From Fig. 1 (b), at low temperatures on winter days, the reflective film is not exposed to the light beam because the VTSS-PCM is in a crystalline opaque state. At this time, the light beam only undergoes the primary reflection (R1) on the surface of VTSS-PCM, and the rest of the light beam is completely absorbed and stored by the VTSS-PCM layer. Thereby, the VTSS-PCM layer can maintain a relatively high temperature and more heat can be transferred into the room through conduction. Through the above analysis, the ABR can regulate solar heat gain in response to changes in ambient temperature to reduce unexpected heat gain or heat loss. Note that affixing the VTSS-PCM externally helps dissipate the heat to the ambient at summer night through longwave radiation and convection, thereby improving the utilization efficiency of its latent heat. However, it also benefits the heat release to the ambient at winter night, which is not good for reducing the heating load.

3. Methodology

This section firstly established the numerical model of ABR, which includes the heat transfer model, optical model, and model solving method. Then, the ABR was experimentally tested under summer and winter conditions, respectively, and the numerical model was validated using the experimental data.

3.1. Numerical model of ABR

3.1.1. Assumptions

In the numerical model, several instructions or assumptions were as follows

(1) Since SS-PCM did not show a flow regime, the phase states of VTSS-PCM were referred to as transparent and opaque, rather than liquid and solid.
(2) When phase transition occurred, the VTSS-PCM was divided into 3 areas: if $T > T_c$, VTSS-PCM was in a transparent state; if $T < T_m$, VTSS-PCM was in an opaque state; if $T_m \leq T \leq T_c$, VTSS-PCM was in a translucent state.
(3) The optical properties (refractive index and extinction coefficient) of each node were assumed to be linear with temperature.
(4) In the optical model, there was no absorptivity on the virtual interface, and the reflectivity on both sides of the interface was equivalent.
(5) The numerical model only considered the heat transfer caused by the temperature difference, ignoring the effects of humidity and precipitation water.

3.1.2. Governing equations

The governing equations of VTSS-PCM and other material layers can be expressed as Eq. (1) and Eq. (2), respectively.

$$\rho_5 C_5 \frac{\partial T}{\partial \tau} = \nabla(\lambda_5 \nabla T) + \nabla(\psi \bullet I) \tag{1}$$

$$\rho_j C_j \frac{\partial T}{\partial \tau} = \nabla(\lambda_j \nabla T) \tag{2}$$

where ρ, C, and λ denote the density, specific heat capacity, and thermal conductivity; τ means the time and T means the temperature; I denotes the solar radiation received by ABR; ψ denotes the solar absorptivity and was modeled in subsection 3.1.4. The subscript 5 denotes the VTSS-PCM, and the subscript j ranges from 1 to 3, representing the outside cement mortar, autoclaved aerated concrete, and inside cement mortar,

respectively. As for the reflective film, only its optical properties are considered.

As shown in Eq. (3), the apparent heat capacity method [26] was used to model the specific heat of VTSS-PCM in different states.

$$C_5 = \begin{cases} C_{o/t} & T < T_m, T > T_c \\ C_{o/t} + \dfrac{Q_l}{T_c - T_m} & T_m \leq T \leq T_c \end{cases} \tag{3}$$

where $C_{o/t}$ is the specific heat of VTSS-PCM in the opaque or transparent state; T_m and T_c are the melting temperature and condensing temperature, respectively; Q_l is the latent heat.

3.1.3. Boundary conditions

At the outer and inner surfaces of ABR, the heat transfer process can be expressed as Eq. (4) and Eq. (5) according to Stefan–Boltzmann law and Newton's law of cooling.

$$-\lambda_5 \frac{\partial T}{\partial x}\Big|_{x=0} = h_o(T_o - T) + h_{sky}(T_{sky} - T) \tag{4}$$

$$-\lambda_3 \frac{\partial T}{\partial x}\Big|_{x=L_t} = h_i(T_i - T) + \varepsilon\sigma(T_i^4 - T^4) \tag{5}$$

where T_i and T_o are the indoor and ambient temperature; T_{sky} is the sky dome temperature, which is the function of T_o Ref. [27]; ε is the infrared emissivity, 0.85; σ is the Stefan-Boltzmann constant; h_{sky} denotes the long-wave radiation heat transfer coefficient between the exterior surface of ABR and the sky dome [28].

The convective heat transfer coefficients in outer and inner surfaces are calculated in Eq. (6) [29] and Eq. (7) [30]. The h_{sky} and h_{sur} are calculated in Eq. (8) and Eq. (9).

$$h_o = max\left\{1.52 \cdot |\Delta T|^{1/3}, 5.62 + 3.9 \cdot v\right\} \tag{6}$$

$$h_i = \frac{2(T_i - T)^{0.32}}{D^{0.04}} \tag{7}$$

$$h_{sky} = \sigma\varepsilon\left(T_{sky}^2 + T^2\right)\left(T_{sky} + T\right) \tag{8}$$

where ΔT is the temperature difference between the indoor air and the interior surface; v is the wind speed; D denotes the distance between the roof and the ground.

3.1.4. The optical model

The visual of the VTSS-PCM varies between transparent and opaque according to the periodic fluctuations of ambient temperature. That is to say, its optical properties change continuously in time and space during the phase transition. Therefore, for the VTSS-PCM, the temperature dependence of the optical properties of each node must be considered. In this study, the VTSS-PCM was divided into N-1 isothermal sub-layers by adding N-2 virtual interfaces. Since the thickness of each sub-layer is thin and isothermal, the optical properties are consistent. During the phase transition, a step-change in the optical properties occurs at each interface. After the phase transition is complete, all sub-layers can be considered as a whole for the calculation. The optical model can accurately calculate the dynamic solar absorptivity of the ABR. The mathematical model is presented in Appendix A. The more detailed optical model of ABR can refer to previous work [25].

3.1.5. Model solving method

In this study, the implicit infinite-difference method was used to discretize the governing equations, and the state-space method [31] was used to address these equations. The time step has a significant impact on the stability of the algorithm. If the time step is set too short, it will significantly increase the calculation cost, especially for the annual performance analysis of ABR. However, if the time step is set too long, the calculation process may directly cross the translucent state of the VTSS-PCM. That is, the temperature of the VTSS-PCM at the previous moment is lower than the melting temperature, but the temperature at the current moment is higher than the condensing temperature. At this time, the application of Eq. (3) will not accurately capture the heat released by the latent heat, and cause numerical oscillations, resulting in the collapse of the calculation process. Therefore, the time step was set to 1 min, and after each time step was over, the node temperature of VTSS-PCM at the current moment was corrected.

Using the time backward implicit finite-difference method to discretize Eq. (1),

$$\rho_5 C_5 T_\tau - \rho_5 C_5 T_{\tau-\Delta\tau} = (\nabla(\lambda_5 \nabla T) + \nabla(\psi \bullet I))\Delta\tau \tag{9}$$

where T_τ and $T_{\tau-\Delta\tau}$ represent the temperature at the current moment and the last moment, respectively.

In the solution process, the state change experienced by each VTSS-PCM node was first judged according to the temperature at the current moment and the previous moment. Then, the algorithm was forced to satisfy the Eq. (9) to recalculate the node temperature at the current moment. During a time step, the node temperature of VTSS-PCM may experience the following conditions. The following formulas were deduced from Eq. (9). Note that if the node of VTSS-PCM is in the same state during a time step, no correction for the node temperature is required.

● The melting process:

$$T_{\tau-\Delta\tau} < T_m < T_\tau < T_c$$

$$\rho\left(C_{o/t} + \frac{Q_l}{T_c - T_m}\right)(T_\tau - T_m) + \rho C_{o/t}(T_m - T_{\tau-\Delta\tau}) = (\nabla(\lambda_5\nabla T) + \nabla(\psi \bullet I))\Delta\tau \tag{10}$$

$$T_{\tau-\Delta\tau} < T_m < T_c < T_\tau,$$

$$\rho C_{o/t}(T_\tau - T_c) + \rho\left(C_{o/t} + \frac{Q_l}{T_c - T_m}\right)(T_c - T_m) + \rho C_{o/t}(T_m - T_{\tau-\Delta\tau}) = (\nabla(\lambda_5\nabla T) + \nabla(\psi \bullet I))\Delta\tau \tag{11}$$

$$T_m < T_{\tau-\Delta\tau} < T_c < T_\tau,$$

$$\rho C_{o/t}(T_\tau - T_c) + \rho\left(C_{o/t} + \frac{Q_l}{T_c - T_m}\right)(T_c - T_{\tau-\Delta\tau}) = (\nabla(\lambda_5\nabla T) + \nabla(\psi \bullet I))\Delta\tau \tag{12}$$
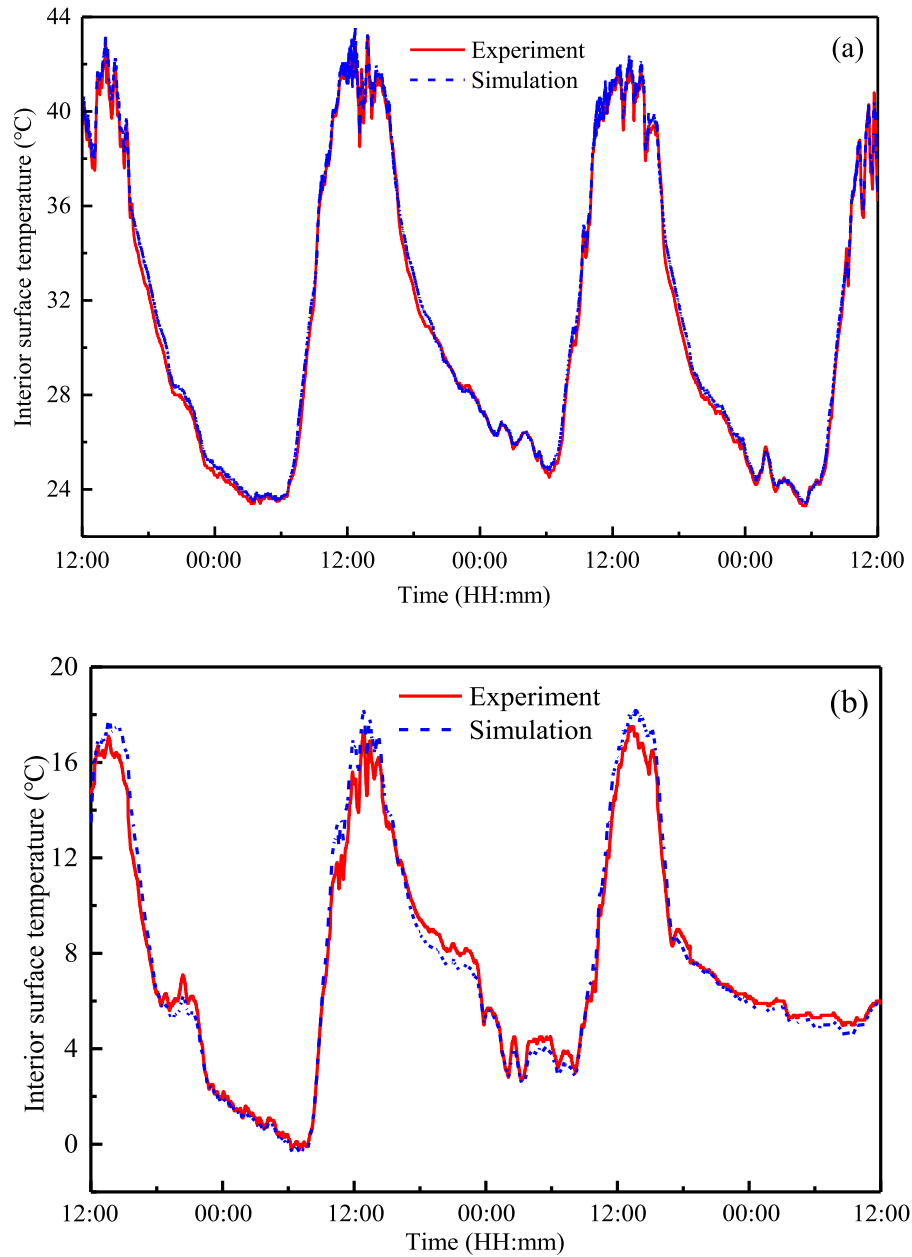
● The melting process:

$$T_\tau < T_m < T_{\tau-\Delta\tau} < T_c$$

Table 1
Materials and geometric properties (Default values) of the ABR for model validation.

Material	d mm	λ W·m⁻¹·K⁻¹	C J·kg⁻¹·K⁻¹	ρ kg·m⁻³	T_m °C	T_c °C	E m⁻¹	Refraction	Reflection	ε
VTSS-PCM	4	0.2	990	800	30	36	50 (transparent) 150 (opaque)	1.5 3	/	0.85
Reflective film	/	/	/	/	/	/	/	/	0.95	/
insulation board	26	0.03	1500	36	/	/	/	/	/	0.85

Fig. 2. Comparison between simulated and experimental values of the interior surface temperature of ABR in (a) summer and (b) winter typical days.

Table 2

Summary statistics from the typical meteorological data in different climate zones [34,35].

	Latitude/ longitude	Köppen-Geiger climate	Monthly average solar radiation range (W/m²)	Monthly average ambient temperature range (°C)	Monthly average wind speed range (m/s)
Beijing	39.8 N/116.47E	Dwa	73.45–211.32	−3.83-26.44	1.93–3.00
Changsha	28.22E/112.92E	Cfa	62.16–197.83	5.54–28.54	1.77–2.59
Guangzhou	23.17 N/ 113.33E	Cwa	82.23–159.66	13.92–28.81	1.47–1.92
Urumqi	43.83 N/87.53E	Bwk	44.65–264.65	−12.33-23.97	1.29–2.93
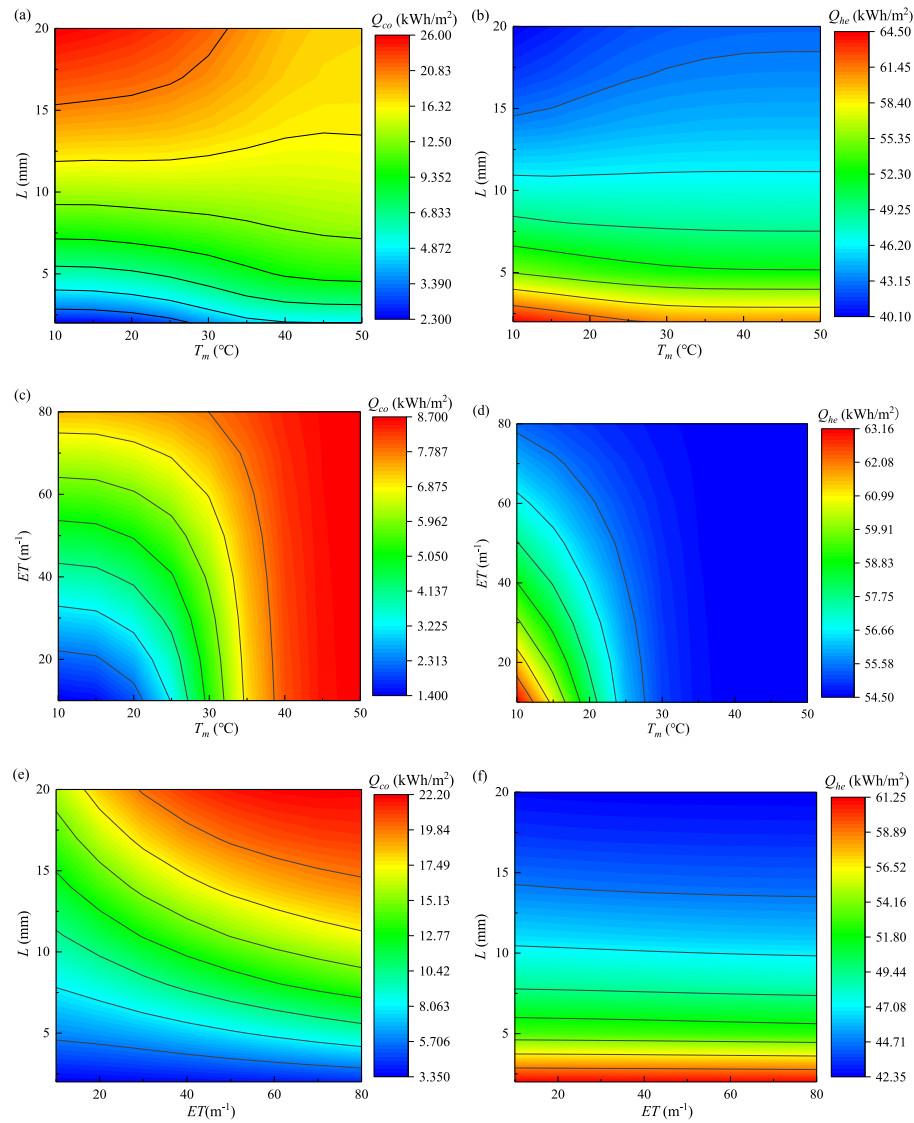
Fig. 3. The combined effect of VTSS-PCM properties on annual cooling load (a, c, e) and annual heating load (b, d, f) of the ABR. (a, b) $T_m \times L$; (c, d) $T_m \times ET$; (e, f) $ET \times L$.
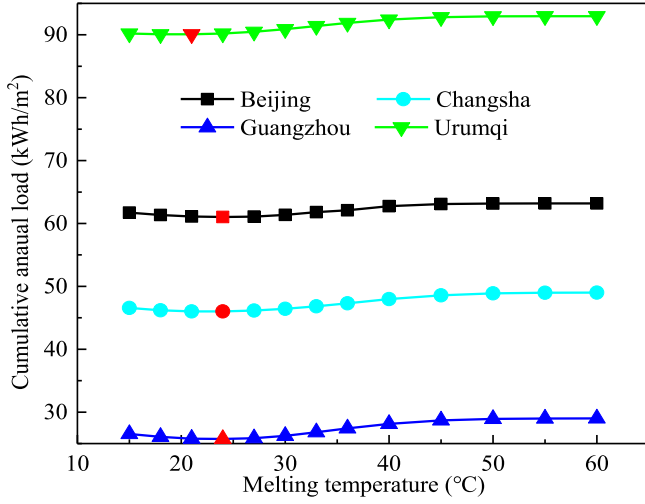
Fig. 4. The CAL of ABR versus melting temperature of VTSS-PCM (optimal values were marked in red). (For interpretation of the references to colour in this figure legend, the reader is referred to the Web version of this article.)

$$\rho C_{o/t}(T_\tau - T_m) + \rho \left(C_{o/t} + \frac{Q_l}{T_c - T_m} \right)(T_m - T_{\tau-\Delta\tau}) = (\nabla(\lambda_5 \nabla T) + \nabla(\psi \bullet I))\Delta\tau \tag{13}$$

$$T_\tau < T_m < T_c < T_{\tau-\Delta\tau},$$

$$T_m < T_\tau < T_c < T_{\tau-\Delta\tau},$$

$$\rho \left(C_{o/t} + \frac{Q_l}{T_c - T_m} \right)(T_\tau - T_c) + \rho C_{o/t}(T_c - T_{\tau-\Delta\tau}) = (\nabla(\lambda_5 \nabla T) + \nabla(\psi \bullet I))\Delta\tau \tag{15}$$

The numerical model was divided into three parts (the main model and two sub-models). The main model calculated the dynamic heat transfer through conduction and convection as well as radiation. The first sub-model described the propagation of solar radiation in the VTSS-PCM and calculated the solar absorptivity by the VTSS-PCM nodes. The second sub-model corrected the temperature of the VTSS-PCM nodes during the phase transition. During computation, the computed values of the two sub-models were fed into the main model. The input parameters include the weather data, thermo-physical and optical parameters of ABR. It is emphasized that after each time step is over, the optical properties of each VTSS-PCM node need to be updated, and the solar absorptivity needs to be recalculated.

3.2. Model validation

In our near work [25], an outdoor test bench with a size of 40 cm × 40 cm × 40 cm was built to initially study the performance of ABR. The ABR in the experiment consists of a VTSS-PCM layer, a reflective film, and an insulation plate. The materials and geometric properties of the ABR are shown in Table 1. In the experiment, the temperature values were measured by Pt100 thermal resistance sensors. The scattered and

$$\rho C_{o/t}(T_\tau - T_m) + \rho \left(C_{o/t} + \frac{Q_l}{T_c - T_m} \right)(T_m - T_c) + \rho C_{o/t}(T_c - T_{\tau-\Delta\tau}) = (\nabla(\lambda_5 \nabla T) + \nabla(\psi \bullet I))\Delta\tau \tag{14}$$
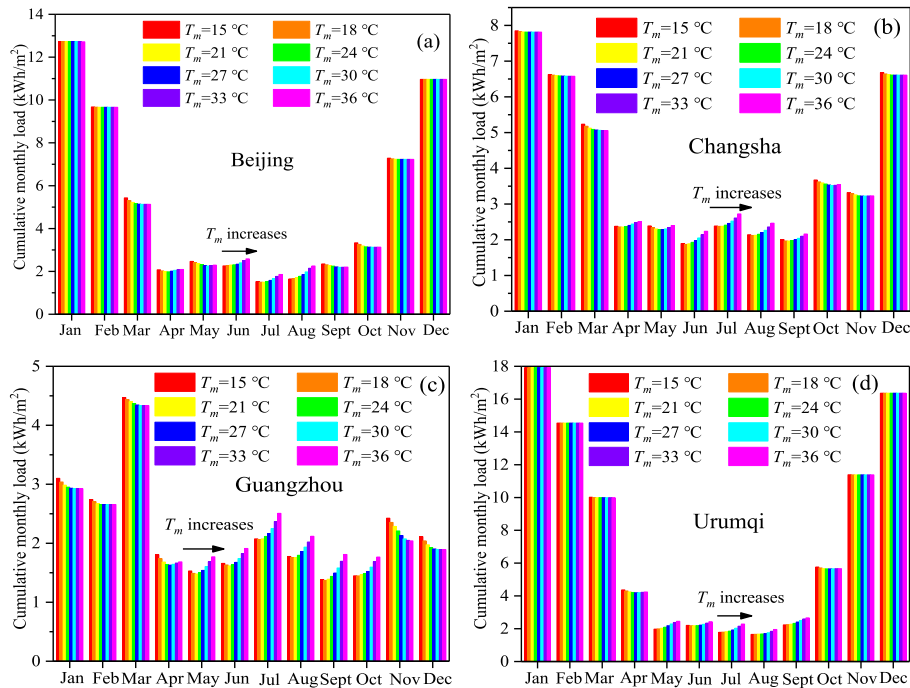
Fig. 5. The CML of ABR versus melting temperature of VTSS-PCM in four cities. (a) Beijing, (b) Changsha, (c) Guangzhou, (d) Urumqi.
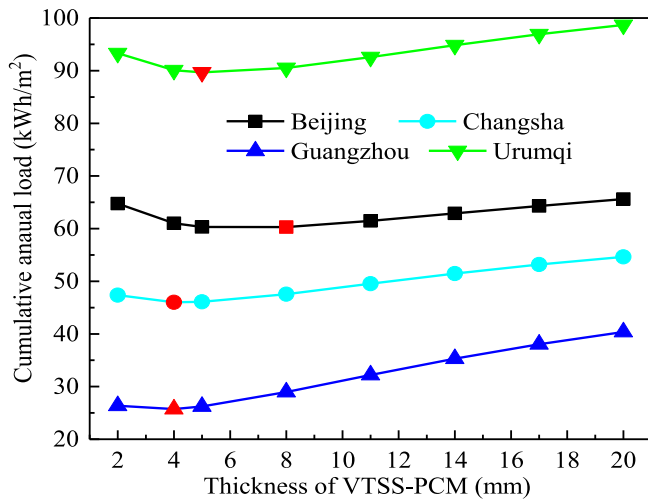
Fig. 6. The CAL of ABR versus thickness of VTSS-PCM (optimal values were marked in red). (For interpretation of the references to colour in this figure legend, the reader is referred to the Web version of this article.)

global solar radiation was measured by TBD-1 and TBQ-2 pyranometers. An anemometer powered by a direct current power supply was used to measure wind speed. The numerical model was verified by the experimental data of three typical days in summer (Sept. 11th-14th) and winter (Jan. 11th-14th), respectively. The meteorological parameters are clearly shown in Appendix B. It was sunny days during the test period, so the effect of the precipitable water was ignored.

Fig. 2(a) and (b) show the comparison results of the simulated and measured values of the interior surface temperature of ABR on summer and winter typical days. Two indicators, the root mean square error (RMSE) and the coefficient of variation (CV) of the RMSE [32], were used to evaluate the reliability of the numerical model. The calculated RMSE and CV(RMSE) were 0.39 °C and 1.27% under summer conditions, and 0.64 °C and 8.5% under winter conditions, respectively. According to the ASHRAE standard [33], the numerical model of ABR had

high accuracy and could be used for the annual performance simulation. From the results, the experimental data of typical winter days were in worse agreement with the simulated data. This was because the proportion of scattered radiation during the winter test was larger. The numerical model assumed that the scattered radiation was uniformly distributed in all directions. However, in practice, the distribution of scattered radiation was random, which was greatly affected by weather conditions.

4. Climate adaptability and energy-saving potential

To evaluate the climate adaptability and energy-saving potential of ABR, four cities located in different climate zones in China were selected: Beijing, Changsha, Guangzhou, and Urumqi. According to the
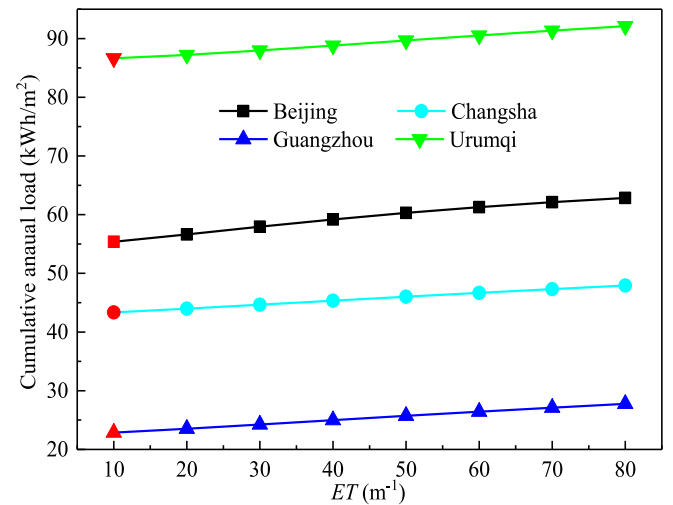
Fig. 8. The CAL of ABR versus the *ET* (optimal values were marked in red). (For interpretation of the references to colour in this figure legend, the reader is referred to the Web version of this article.)
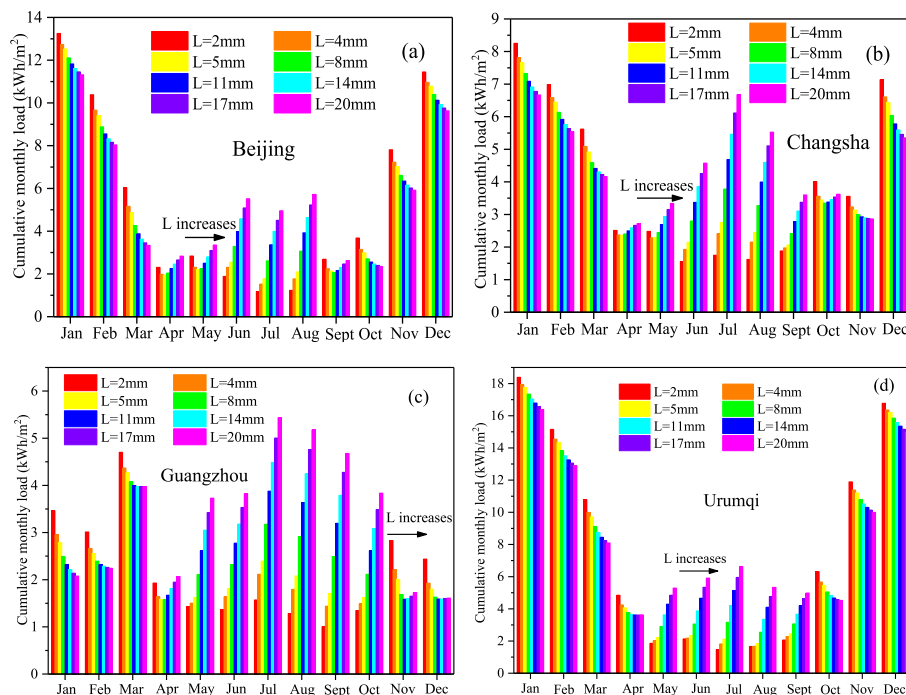
Fig. 7. The CML of ABR versus the thickness of VTSS-PCM in four cities. (a) Beijing, (b) Changsha, (c) Guangzhou, (d) Urumqi.
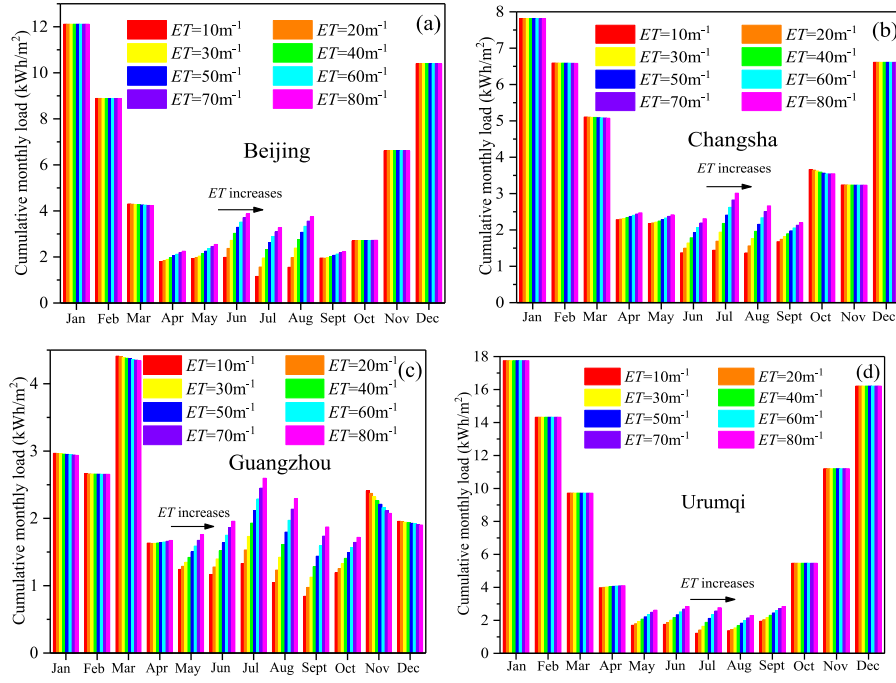
Fig. 9. The CML of ABR versus the *ET* in four cities. (a) Beijing, (b) Changsha, (c) Guangzhou, (d) Urumqi.
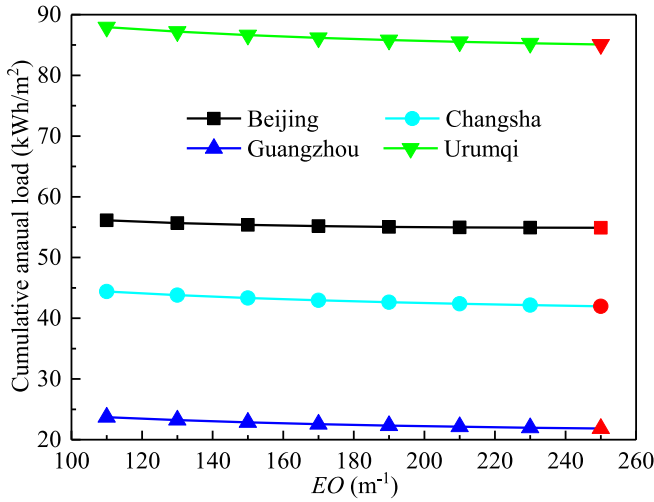

Fig. 10. The CAL of ABR versus the *EO* (optimal values were marked in red). (For interpretation of the references to colour in this figure legend, the reader is referred to the Web version of this article.)

Köppen-Geiger climate classification [34], Beijing is classified as the temperate continental climate (Dwa), Changsha is characterized by the temperature climate with frequent rain (Cfa), and Guangzhou belongs to the temperature climate with summer rain (Cwa). What these three cities have in common is that the average temperature in the hottest month exceeds 22 °C. Urumqi has a desert climate (Bwk), and the average annual temperature is below 18 °C. The typical meteorological year data of the four cities in EnergyPlus [35] were used as simulation input. The summary statistics of typical meteorological data in different climatic regions are shown in Table 2. Note that the indoor temperature was set to 26 °C in the cooling season, 18 °C in the heating season, and 24 °C in the transition season. We considered that the cooling season was when the monthly average temperature exceeded 26 °C, and the heating season was when the monthly average temperature was lower than

18 °C. The rest of the months were transition seasons.

As shown in Eqs. (16) and (17), cooling and heating components due to heat gains and heat losses can be calculated by integrating the heat gains or heat losses over the given period. Therefore, the cumulative monthly/annual load can be expressed as Eq. (18). The sign of the heat loss is a negative value, to facilitate the calculation of the cumulative load, the absolute value of the heating element was taken.

$$Q_{co} = \int_{t=0}^{t=\tau} q_{gain} dt \tag{16}$$

$$Q_{he} = \left| \int_{t=0}^{t=\tau} q_{loss} dt \right| \tag{17}$$

$$Q = Q_{co} + Q_{he} \tag{18}$$

To evaluate the energy-saving potential of ABR in different climate zones, with the CIR as a reference, we defined the following energy-saving rate (ESR) of ABR:

$$ESR = \frac{Q_{CIR} - Q_{ABR}}{Q_{CIR}} \times 100\% \tag{19}$$

5. Results analysis

The parameters of the VTSS-PCM had a combined effect on the performance of ABR. The combined effects of the melting temperature (T_m), thickness (L), and the extinction coefficient of VTSS-PCM in the transparent state (ET) on the annual cooling load and the annual heating load were shown in section 5.1. Considering the variability of the energy performance of ABR in different climate zones, we investigated and optimized the effects of four parameters, including the T_m, L, extinction coefficient of VTSS-PCM (E), and reflectivity of the reflective film (RR), on the seasonal/annual energy performance of ABR in four cities in sections 5.2, 5.3, 5.4, and 5.5, respectively. The typical daily, seasonal and annual dynamic performance was compared between ABR and CIR (without PCM) in section 5.6.
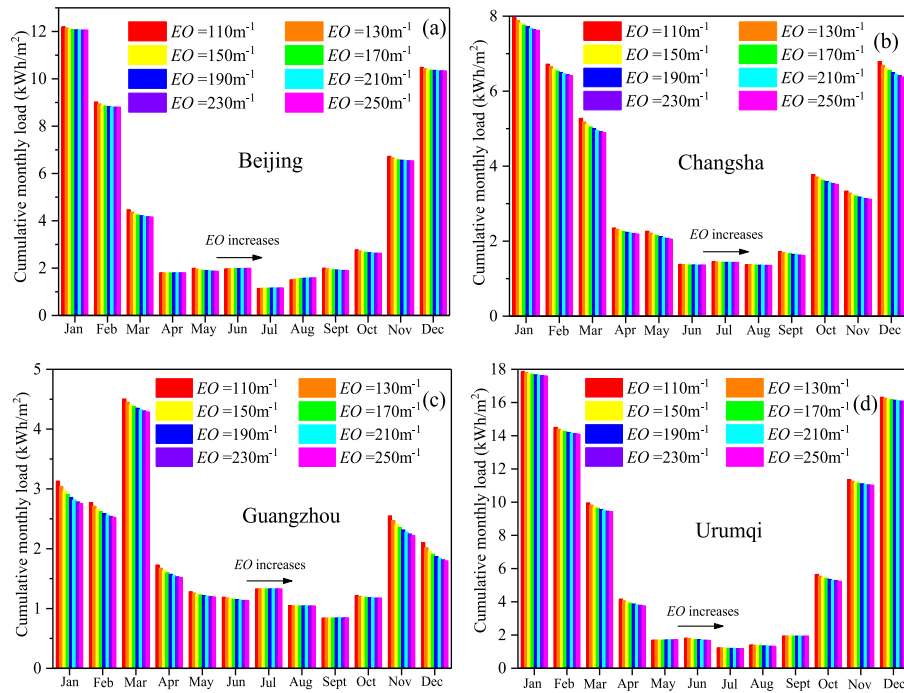
Fig. 11. The CML of ABR versus the *EO* in four cities. (a) Beijing, (b) Changsha, (c) Guangzhou, (d) Urumqi.
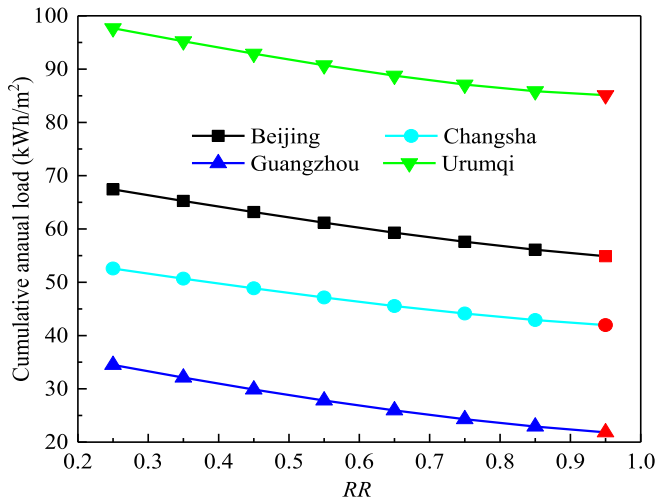

Fig. 12. The CAL of ABR versus the *RR* (optimal values were marked in red). (For interpretation of the references to colour in this figure legend, the reader is referred to the Web version of this article.)

5.1. Combined effect of VTSS-PCM properties

In Beijing climate conditions, the combined effects ($T_m \times L$, $T_m \times ET$, $ET \times L$) on annual cooling load and heating load of the ABR is shown in Fig. 3, from which some conclusions can be drawn:

(1) The decrease of the T_m, L, and ET was beneficial to decrease the annual cooling load, but it also increased the annual heating load. On the one hand, the decrease of T_m made the VTSS-PCM transform into a transparent state at low ambient temperature, and the reflective film reflected more solar radiation. On the other hand, the decrease of L and ET decreased the heat storage of the VTSS-PCM in the transparent state. Therefore, it was necessary to

optimize these parameters to minimize the cumulative annual load (CAL) of the ABR.

(2) From Fig. 3(a) and (b), the combined effect between L and T_m was complex. When the L was less than 10 mm, the increase of T_m increased the annual cooling load and decreased the annual heating load. When the L was larger than 15 mm, the increase of the T_m decreased the annual cooling load and increased the annual heating load. The reason was that, when the L was thinner, the heat storage capacity of VTSS-PCM was limited, and the increase of the T_m decreased the reflectivity of ABR (the VTSS-PCM in an opaque state), and more solar energy was transferred into the indoor through conduction. However, when the L was thicker, the increase of T_m obviously decreased the reflectivity of ABR. At this time, the VTSS-PCM layer stored more solar energy, which was transferred into the ambient through convection and radiation.

(3) From Fig. 3(c) and (d), the higher the T_m, the smaller effect of the ET on the annual cooling and heating load of the ABR. This was because the high T_m caused the VTSS-PCM to remain in an opaque state for a long time, and at this time, the ET had little effect on the heat transfer of ABR.

(4) From Fig. 3(e), the thicker the L, the greater effect of the ET on the annual cooling load. The reason was that the increase of the L increased the propagation path of solar radiation in the VTSS-PCM layer. At this time, the increase of ET led to a greater degree of attenuation of solar radiation. From Fig. 3(f), the combined effect between L and ET on the annual heating load of the ABR was not obvious. This was explained that during the heating season, due to the low ambient temperature, the VTSS-PCM was in an opaque state, thus the ET has little effect on the heating load.

5.2. The impact of melting temperature of VTSS-PCM

Fig. 4 shows the CAL of ABR versus the melting temperature of VTSS-PCM. With the melting temperature increased, the CAL of ABR first decreased, then increased, and finally remained unchanged. The reason was that the influence of the melting temperature of VTSS-PCM on the
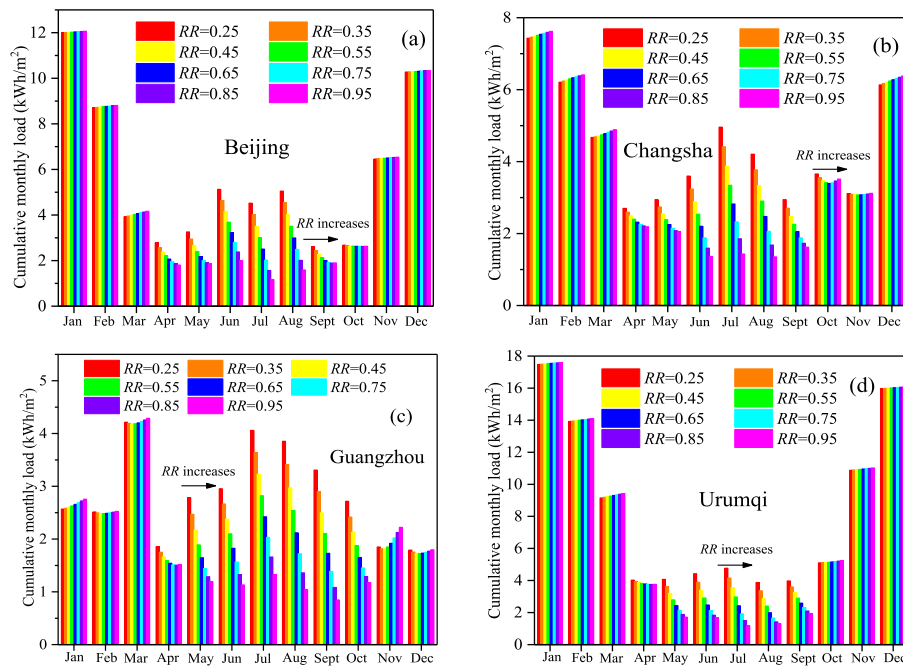
Fig. 13. The CML of ABR versus and the *RR* in four cities. (a) Beijing, (b) Changsha, (c) Guangzhou, (d) Urumqi.

CAL was related to the ambient temperature. Based on ambient temperature, the too low or too high melting temperature was not conducive to improving the utilization of latent heat of VTSS-PCM. The optimal melting temperature of the VTSS-PCM corresponded to the minimum value of the CAL (marked in red). In Beijing, Changsha, and Guangzhou, the optimal melting temperature of VTSS-PCM was 24 °C. At this time, the CALs were 61 kWh/m^2, 46 kWh/m^2, and 26 kWh/m^2, respectively. In Urumqi, the optimal melting temperature of VTSS-PCM was 21 °C, and the corresponding CAL was 90 kWh/m^2. In the following subsections, the melting temperature of VTSS-PCM was set to the optimal value.

Fig. 5 (a), (b), (c), and (d) depict the cumulative monthly load (CML) of ABR versus the melting temperature of VTSS-PCM in four cities. In Beijing and Urumqi, the melting temperature of VTSS-PCM did not affect the CML in the heating season. In contrast, in Changsha and Guangzhou, the CML in the heating season decreased as the melting temperature of VTSS-PCM increased. The reason was that, during the heating season, the ambient temperatures in Beijing and Urumqi were both below 15 °C, and the latent heat of VTSS-PCM was not utilized. However, the ambient temperature in Changsha and Guangzhou fluctuated in the phase transition temperature range of VTSS-PCM. Thus, with the melting temperature increased, the time for VTSS-PCM in the transparent state decreased. The exposure time of the reflective film to solar radiation was reduced, and the solar reflectance of ABR was reduced, resulting in a reduction in the heating load. In the four cities, the CML in the cooling season increased with the melting temperature of VTSS-PCM increased. The reason was that the increase of the melting temperature reduced the utilization rate of the latent heat of the VTSS-PCM. Secondly, the reflectivity of the ABR decreased with the increase of the melting temperature, increasing the cooling load.

In addition, the change of the melting temperature of VTSS-PCM had less effect on the heating season than on the cooling season. This was because in the heating season, although the reflectivity of ABR decreased with the melting temperature increased, the VTSS-PCM layer was fixed on the exterior surface, and the ambient temperature was low. The solar heat gain of VTSS-PCM was released to the ambient through long-wave radiation heat transfer. Thus, the VTSS-PCM had limited heat storage capacity in the heating season.
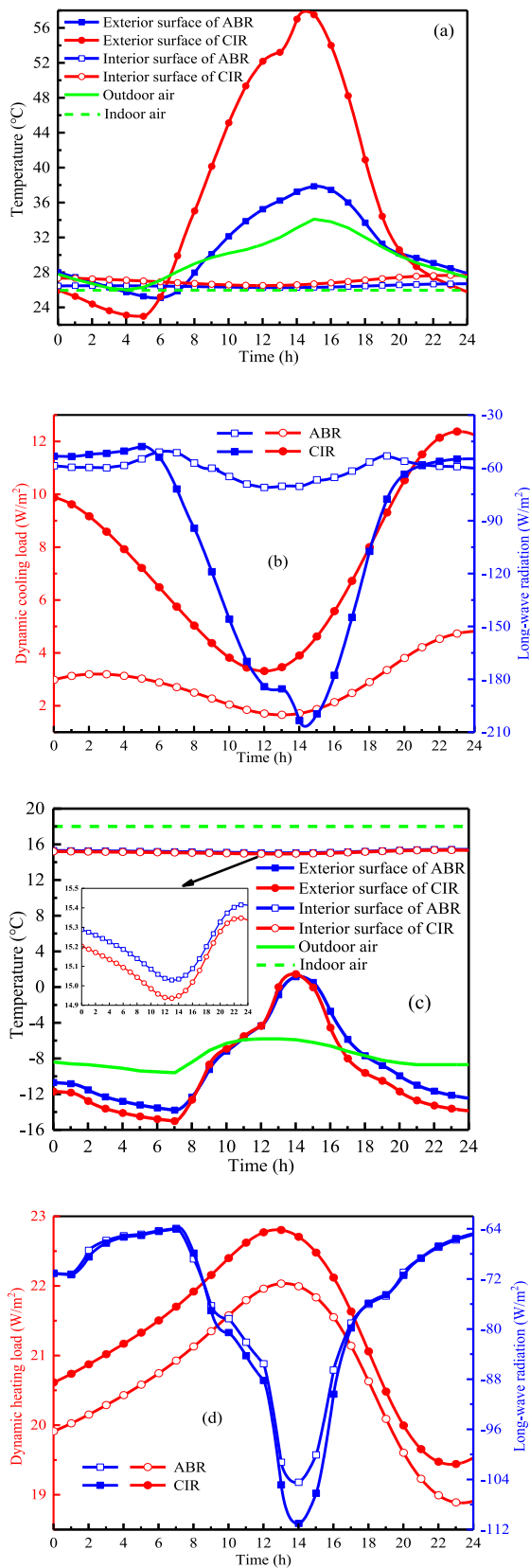
5.3. The impact of the thickness of VTSS-PCM

Fig. 6 shows the CAL of ABR versus the VTSS-PCM thickness. As the thickness increased, the CAL first decreased and then increased. The reason was that the increased thickness of VTSS-PCM helped to reduce the heating load and increase the cooling load. The optimal thickness that minimizes the CAL needed to be weighed during the heating and cooling seasons. The optimal thickness of the VTSS-PCM corresponded to the minimum value of the CAL (marked in red). In Beijing, the optimal thickness of VTSS-PCM was 8 mm, and the corresponding CAL was 60 kWh/m^2. In Changsha and Guangzhou, the optimal thickness of VTSS-PCM was 4 mm, and the corresponding CALs were 46 kWh/m^2 and 26 kWh/m^2. In Urumqi, the optimal thickness of VTSS-PCM was 5 mm, and the corresponding CAL was 90 kWh/m^2. In the following subsections, the thickness of the VTSS-PCM was set to the optimal value.

Fig. 7 (a), (b), (c), and (d) depict the CML of ABR versus the thickness of VTSS-PCM in four cities. With the VTSS-PCM thickness increased, the CML increased significantly in the cooling season, while it decreased significantly in the heating season. The reason was that increasing the thickness of VTSS-PCM not only improved the ability of ABR to absorb and store solar radiation but also reduced the solar reflectance. Compared with the heating season, the change of VTSS-PCM thickness had a more significant impact on the cooling season. Besides, the smaller the thickness of the VTSS-PCM, the more helpful it was to reduce the cooling load. Therefore, the optimal VTSS-PCM thickness did not exceed 8 mm.

5.4. The impact of the extinction coefficient of VTSS-PCM

Fig. 8 shows the CAL of the ABR versus the *ET*. The larger the *ET* meant more solar radiation was converted into heat when passing through the VTSS-PCM layer, thereby increasing the heat entering the room through the ABR. Besides, the VTSS-PCM normally remained transparent during the cooling season. Hence, the change of the *ET* mainly affected the cooling load throughout the year. In Beijing, Changsha, Guangzhou, and Urumqi, the optimal extinction coefficients were all 10 m^{-1} (marked in red), and the corresponding CALs were 55 kWh/m^2, 43 kWh/m^2, 23 kWh/m^2, and 87 kWh/m^2, respectively. In the following subsections, the *ET* was set to the optimal value.

Fig. 9 (a), (b), (c), and (d) depict the CML of ABR versus the *ET* in the four cities. In Beijing, Changsha, and Urumqi, since the fluctuation of ambient temperature was lower than the melting temperature of VTSS-PCM during the heating season, the VTSS-PCM was in an opaque state. Thus the change of *ET* did not affect the heating load. However, in Guangzhou, the melting temperature of VTSS-PCM was in the fluctuation range of ambient temperature during the heating season. Therefore, with the increase of the *ET*, more solar radiation was absorbed during the phase change. During the cooling season, the cooling load of the four cities increased significantly with the *ET* increased. Therefore, from the perspective of the whole year, the smaller the *ET* was helpful to reduce the CAL of ABR.

Fig. 10 shows the CAL of ABR versus the VTSS-PCM extinction coefficient in the opaque state (*EO*) in four cities. The larger the *EO*, the smaller the CAL. In Beijing, Changsha, Guangzhou, and Urumqi, the optimal *EO* were all 250 m^{-1} (marked in red), and the corresponding CALs of ABR were 55 kWh/m^2, 42 kWh/m^2, 22 kWh/m^2, and 85 kWh/m^2. In the following subsections, the *EO* was set to the optimal value.

Fig. 11 (a), (b), (c), and (d) show the CML of ABR versus the *EO* in four cities. In the four cities, the CMLs in both the heating and cooling seasons decreased with the increase of the *EO*. The reason was that, during the heating season, the lower ambient temperature kept the VTSS-PCM opaque, and the larger the *EO* meant that the VTSS-PCM stored more solar radiation, thus improving the thermal insulation of ABR and reducing the heating load. In the cooling season, the ambient temperature fluctuated within the range of the phase transition temperature. Thus, the VTSS-PCM reversibly transformed between the opaque state and the transparent state. During the opaque state of VTSS-PCM, the greater the *EO* meant a faster temperature rise of VTSS-PCM, so the time of VTSS-PCM in the opaque state became shorter, increasing the reflectivity of ABR, thereby reducing the heating load.

5.5. The impact of the RR

Fig. 12 shows the CAL of ABR versus the *RR*. In Beijing, Changsha, Guangzhou, and Urumqi, with the *RR* increased, the CAL decreased. In Beijing, Changsha, Guangzhou, and Urumqi, the optimal *RR* was 0.95 (marked in red), and the corresponding CALs were 55 kWh/m^2, 42 kWh/m^2, 22 kWh/m^2, and 85 kWh/m^2. In the following subsection, the *RR* was set to the optimal value.

Fig. 13 (a), (b), (c), and (d) show the CML of ABR versus and the *RR* in four cities. In the four cities, the CML increased with the increase of the *RR* in the heating season. However, the CML decreased with the increase of the *RR* in the cooling season. The *RR* had less impact on the heating season. The reason was that the ambient temperature fluctuated below the melting temperature of the VTSS-PCM in the heating season, and the VTSS-PCM was in an opaque state. Hence the change in the *RR* had little effect on the reflectivity of ABR. However, in the cooling season, due to the high ambient temperature (especially in Changsha and Guangzhou), the VTSS-PCM was in a transparent state. At this time, increasing the *RR* also obviously increased the reflectivity of the ABR. This also explained that increasing the *RR* helped to reduce the CAL of the ABR.

5.6. Performance comparison between ABR and CIR

This subsection selected two typical days in Beijing, Jul. 15th in summer and Jan. 15th in winter, and compared the dynamic performance of ABR and CIR (without PCM) on both typical days. Furthermore, the monthly and annual performance of ABR and CIR under different climate zones were analyzed and compared.

5.6.1. Typical day performance comparison

Fig. 14(a) shows the temperature distribution of ABR and CIR in Jul. 15th in summer. From Fig. 14(a), the outer surface temperature of CIR was significantly higher than that of ABR during the day. The maximum

Fig. 14. Comparison of temperature distributions and dynamic cooling/heating loads for ABR and CIR on Jul. 15th in summer and Jan. 15th in winter. (a) temperature distribution comparison on Jul. 15th; (b) dynamic cooling load and long-wave radiation comparison on Jul. 15th; (c) temperature distribution comparison on Jan. 15th; (d) dynamic heating load and long-wave radiation comparison on Jan. 15th.
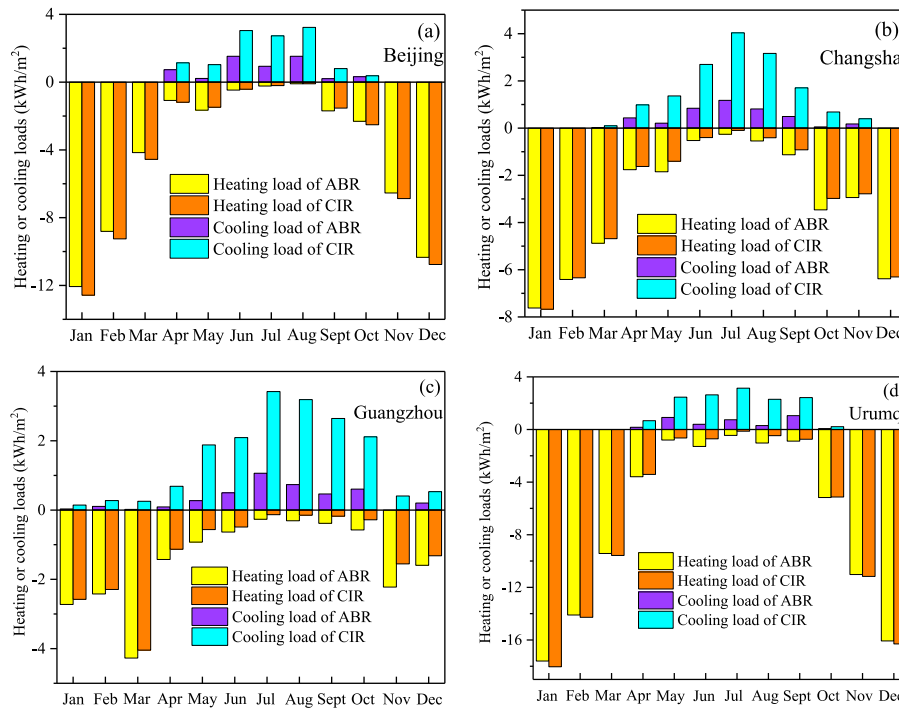
Fig. 15. Comparison of monthly cooling and heating loads between ABR and CIR in the four cities. (a) Beijing, (b) Changsha, (c) Guangzhou, (d) Urumqi.

Table 3
The CML/CAL comparison results of ABR and CIR in the four cities.

Cities		Beijing		Changsha		Guangzhou		Urumqi	
		CIR	ABR	CIR	ABR	CIR	ABR	CIR	ABR
CML (kWh/m²)	Jan.	12.58	12.07	7.62	7.53	**2.69**	**2.76**	17.92	17.60
	Feb.	9.25	8.81	**6.34**	**6.41**	2.57	2.53	14.28	14.10
	Mar.	4.56	4.16	**4.78**	**4.89**	4.30	4.27	9.58	9.43
	Apr.	2.42	1.81	2.61	2.19	1.82	1.52	4.09	3.76
	May	2.51	1.87	2.87	2.16	2.44	1.19	3.10	1.72
	Jun.	3.46	1.99	3.19	1.37	2.48	1.13	3.24	1.67
	Jul.	2.54	1.17	4.16	1.43	3.55	1.33	3.17	1.18
	Aug.	3.29	1.70	3.58	1.36	3.24	1.04	2.77	1.33
	Sept.	2.33	1.90	2.63	1.62	2.72	0.85	3.07	1.94
	Oct.	2.89	2.63	3.66	3.52	2.39	1.18	5.34	5.24
	Nov.	6.87	6.54	3.18	3.12	**1.96**	**2.32**	11.17	11.02
	Dec.	10.76	10.34	**6.31**	**6.38**	1.85	1.80	16.30	16.05
CAL (kWh/m²)		64	55	51	42	32	22	94	85
ESR (%)		14.06		17.65		31.25		9.57	

exterior surface temperature of CIR reached 58 °C, while the maximum exterior surface temperature of the ABR was only 38 °C. Besides, the average inner surface temperature of the CIR was 0.60 °C higher than that of the ABR. Fig. 14(b) shows the dynamic cooling load and the long-wave radiation heat exchange of ABR and CIR in Jul. 15th. From Fig. 14 (b), the dynamic cooling load of CIR was always larger than that of ABR. The average daily cooling load of CIR was 7.24W/m², while that of ABR was 2.87 W/m². Therefore, the ABR had better heat insulation performance in summer. The impact of long-wave radiation from the atmosphere was always present on the ABR surface. A negative value for long-wave radiation meant that the envelope surface emitted heat rays to the ambient. Compared to CIR, the ABR released more radiant heat to the sky at night to freeze the VTSS-PCM layer, which aided heat storage for the next day. Because the exterior surface temperature of CIR was higher than that of ABR during the daytime, the CIR emitted more heat rays to the ambient.

Fig. 14(c) shows the temperature distribution of ABR and CIR on Jan. 15th in winter. Compared to CIR, the fluctuation of the outer surface temperature of ABR had attenuation and delay because the VTSS-PCM

stored the solar energy. On the winter day, the average inner surface temperature of the ABR was 0.10 °C higher than that of the CIR. Fig. 14 (d) shows the dynamic heating load and the long-wave radiation heat exchange of ABR and CIR on Jan. 15th. The dynamic heating load of CIR was always larger than that of ABR. The average daily heating load of CIR was 21.34W/m², while that of ABR was 20.68 W/m². Therefore, the ABR had better heat preservation performance in winter. From Fig. 14 (d), the ABR released less radiant heat to the sky during the daytime, which reduced the heat loss. However, the amount of the long-wave radiation of ABR was close to that of CIR at night. It would be even better if the ABR always released less radiant heat into the sky on a winter night.

5.6.2. Seasonal and annual performance comparison

Fig. 15 shows the comparison results of monthly cooling and heating loads between ABR and CIR in the four cities. The heating load was set below the zero scale line to analyze the monthly cooling load and the monthly heating load between ABR and CIR, respectively. In Beijing (Dwa) and Urumqi (Bwk), adopting the ABR helped to reduce both

monthly cooling and monthly heating loads. The reason was that, in the Dwa and Bwk climates, the fluctuation of the ambient temperature caused the VTSS-PCM to transform into a transparent state in the cooling season but kept opaque in the heating season. Note that in the heating season, the energy-saving performance of ABR was not apparent. The reason was that the VTSS-PCM was fixed on the exterior surface of the ABR, and the ambient temperature in Beijing and Urumqi was lower in the heating season, so the heat stored in the VTSS-PCM was released into the ambient through long-wave radiation heat transfer. To further improve the energy-saving performance of ABR, future research should focus on reducing the long-wave radiation heat transfer of VTSS-PCM with the ambient during the heating season.

In Changsha (Cfa) and Guangzhou (Cwa), the adoption of ABR significantly reduced the monthly cooling load but slightly increased the monthly heating load. The reason was that, in the Cfa and Cwa climates, the VTSS-PCM was in a transparent state in the cooling season, while the fluctuation of the ambient temperature in the heating season also caused the partial melting of the VTSS-PCM, which in turn slightly increased the reflectivity of the ABR. It can be found that the problem with using PCMs to passively regulate the solar heat gain of the building envelope was that the triggering mechanism of the energy storage in PCMs cannot be controlled (e.g. the melting temperature of PCM cannot be changed in summer and winter). Thus, it was difficult to find a configuration that works well all year round, especially in climatic zones with large fluctuations in ambient temperature in summer and winter.

Table 3 shows the CML/CAL comparison results of ABR and CIR in the four cities. In Beijing and Urumqi, the CML of ABR was consistently lower than that of CIR. In Changsha and Guangzhou, the ABR also showed better performance. However, the CML of ABR was larger than that of CIR in some heating months, such as Feb., Mar., and Dec. in Changsha and Jan. and Nov. in Guangzhou (in bold). The results showed that, compared with the CIR, the application of ABR achieved the building energy efficiency in the four cities. The ESRs in Beijing, Changsha, Guangzhou, and Urumqi was 13.91%, 17.22%, 32.40%, and 9.80%, respectively. Therefore, the ABR had better energy-saving performance in Cfa and Cwa climate zones.

6. Conclusions

In this study, an ABR was proposed by utilizing the variable transparency characteristics of shape-stabilized PCM. A mathematical model of ABR was developed and verified by experiments in summer and winter conditions. On this basis, the impact of four factors on the performance of ABR was investigated and optimized. The energy performance was compared between ABR and CIR on a typical day, season, and year. The major findings are as follows:

(1) The established mathematical model of ABR considered the dependence of the optical parameters of VTSS-PCM on temperature, and experiments in summer and winter conditions verified the model. The RMSE and CV(RMSE) values indicated the reliability of the model.

(2) The melting temperature, thickness, extinction coefficient of VTSS-PCM, and the reflectivity of the reflective film had a vital influence on the performance of ABR. The optimal melting temperature and thickness of VTSS-PCM were 24 °C and 8 mm in Beijing, 24 °C and 4 mm in Changsha and Guangzhou, and 21 °C and 5 mm in Urumqi. In the four cities, the optimal extinction coefficients of VTSS-PCM in the transparent/opaque state were 10 m^{-1} and 250m^{-1} and the optimal reflectivity of the reflective film was 0.95.

(3) Compared with CIR, the ABR had better heat insulation performance in summer and better heat preservation performance in winter. In Beijing, Changsha, Guangzhou, and Urumqi, the CALs were 55 kWh/m^2, 42 kWh/m^2, 22 kWh/m^2, and 85 kWh/m^2, respectively. The corresponding ESRs of ABR were 14.06%, 17.65%, 31.25%, and 9.57%. The ABR had better energy performance in Cfa and Cwa climate areas.

(4) In different climate zones, the ABR had good performance in the cooling season, but the performance was not good enough in the heating season. In Dwa and Bwk climate zones, the stored solar energy by the VTSS-PCM was released to the ambient through long-wave radiation and convection. In Cfa and Cwa climate zones, the fluctuation of ambient temperature during the heating season led to an increase of the reflectivity of ABR. Future research should further improve the energy-saving potential of ABR by reducing the heat transfer capacity of VTSS-PCM with the ambient during the heating season.

CRediT authorship contribution statement

Pengcheng Wang: Writing – original draft, Visualization, Validation, Software, Methodology, Investigation, Formal analysis, Data curation, Conceptualization. **Zhongbing Liu:** Writing – review & editing, Supervision, Methodology, Funding acquisition, Conceptualization. **Xiaoyang Zhang:** Visualization, Validation, Data curation. **Hangming Zhang:** Validation, Investigation, Data curation. **Xi Chen:** Writing – review & editing. **Ling Zhang:** Writing – review & editing, Supervision, Methodology.

Declaration of competing interest

The authors declare that they have no known competing financial interests or personal relationships that could have appeared to influence the work reported in this paper.

Data availability

No data was used for the research described in the article.

Acknowledgment

Appendix A

At each interface, Eq. (A.1)-Eq. (A.3) can be obtained according to the energy balance.

$$G_k^{'} + F_k = G_k + F_k^{'} \tag{A.1}$$

$$G_k^{'} = (1 - r_k) \bullet G_k + r_k \bullet F_k^{'} \tag{A.2}$$

$$F_k = r_k \bullet G_k + (1 - r_k) \bullet F_k^{'} \tag{A.3}$$

where r_k is the reflectivity of interface k, which relates to the angle of incidence and the refractive index [36].

In each isothermal sub-layer of the VTSS-PCM, the transmittance can be calculated by Eq. (A.4) and Eq. (A.5) simultaneously. Eq. (A.4) is written according to the definition of transmittance, while (A.5) is derived from the Beer-Lambert law.

$$\xi_{k \to k+1} = G_{k+1} / G'_k = F'_k / F_{k+1} \tag{A.4}$$

$$\xi = \frac{I_{out}}{I_{in}} = exp(-E \cdot dx / cos\,\theta) \tag{A.5}$$

where E is the extinction coefficient; θ is the angle of refraction; dx is the physical thickness.

The forward equivalent transmittance ($\alpha_k = G'_k/G_k$), forward equivalent reflectivity ($\beta_k = F_k/G_k$), and reciprocal of the reverse equivalent reflectivity ($\beta'_k = F'_k/G'_k$) are defined as intermediate parameters. Combining formulas (A.6)-(A.8), these parameters can be derived as

$$\alpha_k = (1 - r_k) / (1 - r_k \bullet \beta'_k) \tag{A.6}$$

$$\beta_k = 1 - \alpha_k \bullet (1 - \beta'_k) \tag{A.7}$$

$$\beta'_k = \beta_{k+1} \bullet \xi^2_{k \to k+1} \tag{A.8}$$

From formulas (A.6)-(A.8), if the reflectance of the last sub-layer is known, the equivalent transmittance of each sub-layer of VTSS-PCM can be derived. Then, the solar heat gain of the sub-layer can be calculated as

$$Q_{k \to k+1} = \Delta G_{k \to k+1} + \Delta F_{k+1 \to k} = G'_k \bullet (1 - \xi_{k \to k+1}) + F'_k \bullet \left(\frac{1 - \xi_{k \to k+1}}{\xi_{k \to k+1}} \right) \tag{A.9}$$

In direct radiation, the solar absorptivity of each transparent sub-layer can be obtained by combining Eqs. (A.6)-(A.9).

$$\psi(\theta)_{k \to k+1} = \prod_{m=1}^{k-1} (\alpha_i \bullet \xi_{m \to m+1}) \bullet \alpha_k \bullet \left[(1 - \xi_{k \to k+1}) + \beta'_k \bullet \frac{(1 - \xi_{k \to k+1})}{\xi_{k \to k+1}} \right] \tag{A.10}$$

Unlike the other transparent interfaces, the solar absorptivity of the opaque interface N can be expressed Eq. (A.11) in the direct radiation

$$\psi(\theta)_N = \prod_{m=1}^{N-1} (\alpha_m \bullet \xi_{m \to m+1}) \bullet (1 - r_N) \tag{A.11}$$

The scattered radiation is assumed to be consistent in all directions. Thus, as shown in Eq. (A.12), the solar absorptivity can be calculated by integrating within the range of the incident angle.

$$\psi_{s,k \to k+1} = \frac{2 \int_{0}^{\pi/2} \alpha(\theta)_{k \to k+1} \bullet I_s d\theta}{2 \int_0^{\pi/2} I_s d\theta} \tag{A.12}$$

Appendix B

Fig. B.1 shows the weather data on Sept. 11th-14th in the summer test. Fig. B.2 shows the meteorological data on Jan. 11th-14th in the winter test. The weather data includes outdoor temperature, indoor temperature, global solar radiation, and wind speed. Note that since the test facility was sealed during the test, the ambient temperature was lower than the indoor temperature during the day.
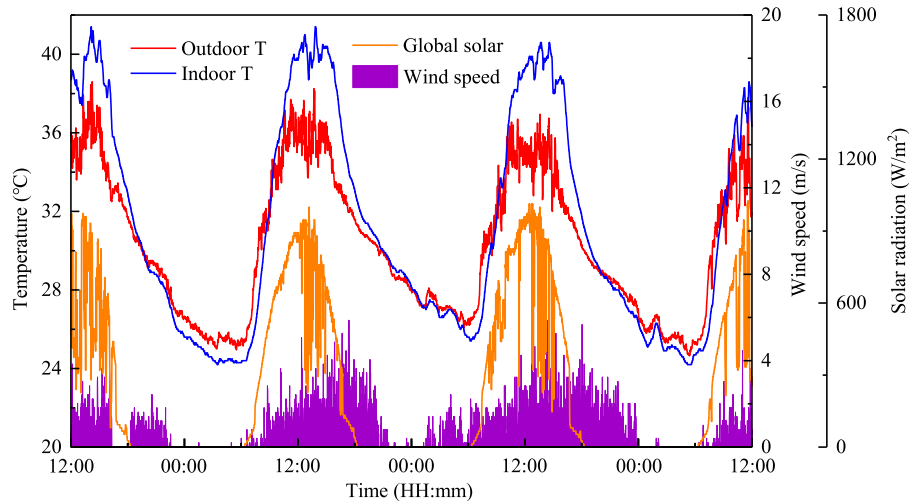

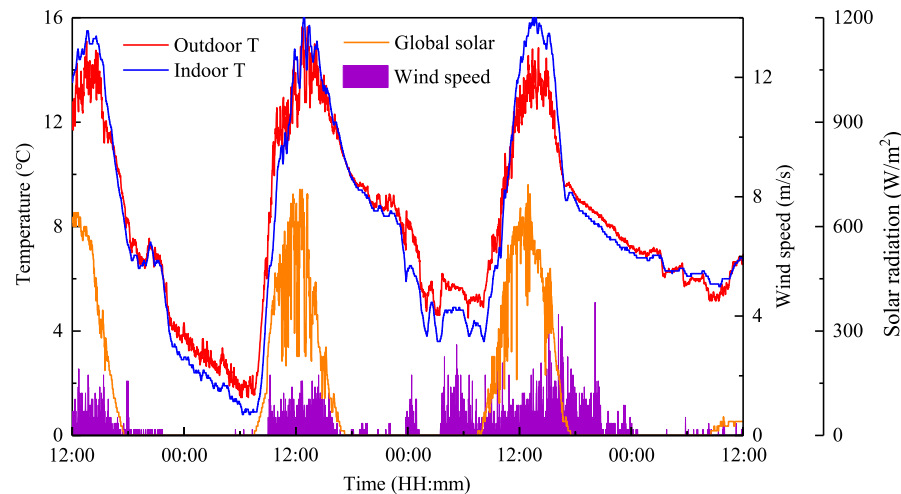**Fig. B.1.** The weather data was recorded during three summer typical days (Sept. 11th −14th).

Fig. B.2. The weather data was recorded during the three winter typical days (Jan. 11th-14th).

References

[1] International Energy Agency, n.d, https://www.iea.org/data-and-statistics?country=WORLD%26fuel=Energy%2520supply%26indicator=TPESbySource, 2021.

[2] Z. Wu, L. Zhang, J. Wu, Z. Liu, Experimental and numerical study on the annual performance of semi-transparent photovoltaic glazing in different climate zones, Energy (2022), https://doi.org/10.1016/j.energy.2021.122473.

[3] P. Wang, Z. Liu, L. Zhang, Sustainability of compact cities: a review of Inter-Building Effect on building energy and solar energy use, Sustain. Cities Soc. 72 (2021), 103035, https://doi.org/10.1016/J.SCS.2021.103035.

[4] N. Moazzen, M.E. Karagüler, T. Ashrafian, Comprehensive parameters for the definition of nearly zero energy and cost optimal levels considering the life cycle energy and thermal comfort of school buildings, Energy Build. (2021), https://doi.org/10.1016/j.enbuild.2021.111487.

[5] A. Ghosh, B. Norton, Advances in switchable and highly insulating autonomous (self-powered) glazing systems for adaptive low energy buildings, Renew. Energy (2018), https://doi.org/10.1016/j.renene.2018.04.038.

[6] A. Tabadkani, A. Roetzel, H.X. Li, A. Tsangrassoulis, Design approaches and typologies of adaptive facades: a review, Autom. ConStruct. (2021), https://doi.org/10.1016/j.autcon.2020.103450.

[7] R.C.G.M. Loonen, M. Trčka, D. Cóstola, J.L.M. Hensen, Climate adaptive building shells: state-of-the-art and future challenges, Renew. Sustain. Energy Rev. 25 (2013) 483–493, https://doi.org/10.1016/J.RSER.2013.04.016.

[8] M. Royapoor, A. Antony, T. Roskilly, A review of building climate and plant controls, and a survey of industry perspectives, Energy Build. (2018), https://doi.org/10.1016/j.enbuild.2017.10.022.

[9] H. Alkhatib, P. Lemarchand, B. Norton, D.T.J. O'Sullivan, Deployment and control of adaptive building facades for energy generation, thermal insulation, ventilation and daylighting: a review, Appl. Therm. Eng. (2021), https://doi.org/10.1016/j.applthermaleng.2020.116331.

[10] Q. Jin, X. Long, R. Liang, Numerical analysis on the thermal performance of PCM-integrated thermochromic glazing systems, Energy Build. 257 (2022), 111734, https://doi.org/10.1016/J.ENBUILD.2021.111734.

[11] R.D. Beltrán, J. Martínez-Gómez, Analysis of phase change materials (PCM) for building wallboards based on the effect of environment, J. Build. Eng. 24 (2019), 100726, https://doi.org/10.1016/J.JOBE.2019.02.018.

[12] A.H.A. Dehwah, M. Krarti, Control strategies for switchable roof insulation systems applied to US residential homes, Energy Build. (2021), https://doi.org/10.1016/j.enbuild.2020.110649.

[13] Y. Luo, L. Zhang, Z. Liu, J. Wu, Y. Zhang, Z. Wu, et al., Performance analysis of a self-adaptive building integrated photovoltaic thermoelectric wall system in hot summer and cold winter zone of China, Energy (2017), https://doi.org/10.1016/j.energy.2017.09.015.

[14] A.H.A. Dehwah, M. Krarti, Impact of switchable roof insulation on energy performance of US residential buildings, Build. Environ. (2020), https://doi.org/10.1016/j.buildenv.2020.106882.

[15] L. Xu, L. Dai, L. Yin, X. Sun, W. Xu, R. Yang, et al., Research on the climate response of variable thermo-physical property building envelopes: a literature review, Energy Build. (2020), https://doi.org/10.1016/j.enbuild.2020.110398.

[16] R.A. Kishore, M.V.A. Bianchi, C. Booten, J. Vidal, R. Jackson, Parametric and sensitivity analysis of a PCM-integrated wall for optimal thermal load modulation in lightweight buildings, Appl. Therm. Eng. (2021), https://doi.org/10.1016/j.applthermaleng.2021.116568.

[17] W. Li, W. Chen, Numerical analysis on the thermal performance of a novel PCM-encapsulated porous heat storage Trombe-wall system, Sol. Energy (2019), https://doi.org/10.1016/j.solener.2019.06.052.

[18] J. Hu, Yu X (Bill), Adaptive building roof by coupling thermochromic material and phase change material: energy performance under different climate conditions, Construct. Build. Mater. (2020), https://doi.org/10.1016/j.conbuildmat.2020.120481.

[19] Y. Qiao, L. Yang, J. Bao, Y. Liu, J. Liu, Reduced-scale experiments on the thermal performance of phase change material wallboard in different climate conditions, Build. Environ. (2019), https://doi.org/10.1016/j.buildenv.2019.106191.

[20] Y. Zhou, C.W.F. Yu, G. Zhang, Study on heat-transfer mechanism of wallboards containing active phase change material and parameter optimization with ventilation, Appl. Therm. Eng. (2018), https://doi.org/10.1016/j.applthermaleng.2018.04.083.

[21] P.K.S. Rathore, S.K. Shukla, Enhanced thermophysical properties of organic PCM through shape stabilization for thermal energy storage in buildings: a state of the art review, Energy Build. (2021), https://doi.org/10.1016/j.enbuild.2021.110799.

[22] Y. Yang, W. Wu, S. Fu, H. Zhang, Study of a novel ceramsite-based shape-stabilized composite phase change material (PCM) for energy conservation in buildings, Construct. Build. Mater. (2020), https://doi.org/10.1016/j.conbuildmat.2020.118479.

[23] P. Mishra, K. Stockmal, G. Ardito, M. Tao, S. Van Dessel, S. Granados-Focil, Thermo-optically responsive phase change materials for passive temperature regulation, Sol. Energy (2020), https://doi.org/10.1016/j.solener.2019.12.064.

[24] G. Guldentops, G. Ardito, M. Tao, S. Granados-Focil, S. Van Dessel, A numerical study of adaptive building enclosure systems using solid–solid phase change materials with variable transparency, Energy Build. (2018), https://doi.org/10.1016/j.enbuild.2018.02.054.

[25] P. Wang, Z. Liu, S. Xi, Y. Zhang, L. Zhang, Experiment and numerical simulation of an adaptive building roof combining variable transparency shape-stabilized PCM, Energy Build. (2022), 112030, https://doi.org/10.1016/J.ENBUILD.2022.112030.

[26] Y. Khattari, T. El Rhafiki, N. Choab, T. Kousksou, M. Alaphilippe, Y. Zeraouli, Apparent heat capacity method to investigate heat transfer in a composite phase change material, J. Energy Storage (2020), https://doi.org/10.1016/j.est.2020.101239.

[27] K.S. Ong, A mathematical model of a solar chimney, Renew. Energy (2003), https://doi.org/10.1016/S0960-1481(02)00057-5.

[28] F. Goia, M. Perino, M. Haase, A numerical model to evaluate the thermal behaviour of PCM glazing system configurations, Energy Build. (2012), https://doi.org/10.1016/j.enbuild.2012.07.036.

[29] G.V. Fracastoro, L. Gai MP, Reducing Cooling Loads with under Roof Air Cavities, Proc. 18th AIVC Conf., Athens, Greece, 1997, pp. 477–486.

[30] T.C. Min, L.F. Schutrum, G.V. Parmelee JDV, Natural convection and ra- diation in a panel heated room, Heat. Pip. Air Cond. (1956) 153–160.

[31] K. Ouyang, F. Haghighat, A procedure for calculating thermal response factors of multi-layer walls-State space method, Build. Environ. (1991), https://doi.org/10.1016/0360-1323(91)90024-6.

[32] Pengcheng Wang, Zhongbing Liu, Dapeng Chen, Weijiao Li, Ling Zhang, Experimental study and multi-objective optimisation of a novel integral thermoelectric wall, Energy Build. (2021) 252.

[33] P. Wang, Z. Liu, D. Chen, W. Li, L. Zhang, Experimental study and multi-objective optimisation of a novel integral thermoelectric wall, Energy Build. 252 (2021), 111403, https://doi.org/10.1016/J.ENBUILD.2021.111403.

[34] http://koeppen-geiger.vu-wien.ac.at/applications.htm n.d.

[35] EnergyPlus. https://energyplus.net/weather n.d.

[36] Y. Liu, Y. Chen, S. Zheng, Y. Li, B. Lu, M. Lu, et al., A model and method to determine solar extinction coefficient of aerogel granules layer through experiment under real climatic condition, Energy Build. (2019), https://doi.org/10.1016/j.enbuild.2019.02.032.